

PHASE SPACE SKETCHING FOR CRYSTAL IMAGE ANALYSIS BASED ON SYNCHROSQUEEZED TRANSFORMS

HAIZHAO YANG AND JIANFENG LU

ABSTRACT. Recent developments of imaging techniques enable researchers to visualize materials at the atomic resolution to better understand the microscopic structures of materials. This paper aims at automatic and quantitative characterization of potentially complicated microscopic crystal images, providing feedback to tweak theories and improve synthesis in materials science. As such, an efficient phase-space sketching method is proposed to encode microscopic crystal images in a translation, rotation, illumination, and scale invariant representation, which is also stable with respect to small deformations. Based on the phase-space sketching, we generalize our previous analysis framework for crystal images with simple structures to those with complicated geometry.

1. INTRODUCTION

Crystal image analysis at the atomic resolution has become an important research direction in materials science recently [1, 23, 3, 30, 13]. The advancement of image acquisition techniques enable researchers to visualize materials at atomic resolution, with images of clearly visible individual atoms and their types (see Figure 1 (a)) and defects such as dislocations and grain boundaries (see Figure 1 (f)). These high-resolution images provide unprecedented opportunities to characterize and study the structure of materials at the microscopic level, which is crucial for designing new materials with functional properties.

The recognition of important quantities and active mechanisms (e.g., dislocations, grain boundaries, grain orientation, deformation, cracks) in a material requires the use of automatic and quantitative analysis by computers. Due to the extraordinarily large volume of measurements and simulations in daily research activities (see Figure 1), in particular, in the case of analyzing a time series of crystal images during the dynamic evolution of crystallization [19], crystal melting [16, 18], solid-solid phase transition [17], and self-assembly [6] etc., it is impractical to analyze these images manually. In the case of crystal images with complicated geometry (see Figure 1 (b) for an example), it becomes difficult to recognize and parametrize the image patterns by visual inspection. Moreover, it is also difficult,

Date: November 4, 2022.

Key words and phrases. Atomic resolution crystal image, phase-space sketching, 2D synchrosqueezed transform, transformation invariance, texture classification, image segmentation.

This work was supported in part by the National Science Foundation under awards DMS-1454939 and ACI-1450372. H.Y. also thanks the support from the AMS-Simons Travel Award. We would like to thank Yilong Han and Yang Xiang for helpful discussions.

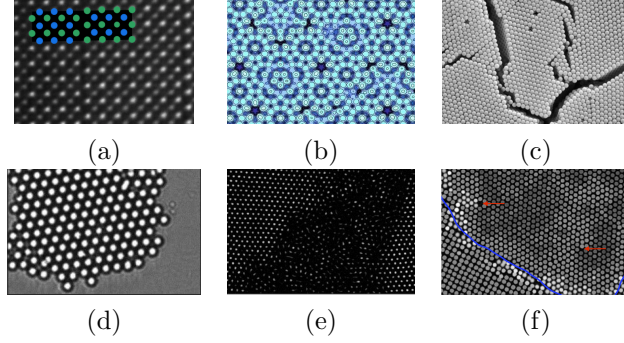


FIGURE 1. (a) A colorized sub-Angstrom scanning transmission electron microscope image clearly shows individual atomic columns of strontium (green), titanium (blue), and oxygen (red) [22]. Courtesy of Greg Stone of Pennsylvania State University. (b) Potential energy surface for silver depositing on an aluminium-palladium-manganese (Al-Pd-Mn) quasicrystal surface. Similar to Figure 6 in [25]. (c) Colloidal crystal with a crack in self-assembly [6]. Courtesy of Aizenberg et al. at Harvard University. (d) An optical microscopy image of electric field mediated colloidal crystallization in fluid [8]. Courtesy of Edwards et al.. (e) Melting behaviors of thin crystalline films [18]. Courtesy of Yilong Han of Hong Kong University of Science and Technology, and Arjun Yodh of Pennsylvania State University. (f) A microscopic image showing the simulation of nucleation mechanism in solidsolid phase transitions [17]. Courtesy of Yilong Han of Hong Kong University of Science and Technology, and Arjun Yodh of Pennsylvania State University. Examples of dislocations are pointed out by red arrows and grain boundaries are indicated in blue.

if not impossible, to measure crystal deformation directly from crystal images by hand. Therefore, there is a dire need for efficient tools to classify and analyze atomic resolution crystal images automatically and quantitatively, with minimal human intervention.

There have been several types of methods for atomic resolution crystal image analysis, assuming simple crystal patterns are known a priori, typically a hexagonal or a square reference lattice in two dimensions (see Figure 2). One class of methods tries to estimate atom positions first (or assume knowledge of the atom positions), and then compute the local lattice orientation and deformation as well as defects via identifying the nearest neighbors of each atom [24]. Other methods are based on a local, direction sensitive frequency analysis, e.g. wavelets [21] to segment the crystal image into several crystal grains and identify their orientations. Another more advanced class of methods formulates the crystal analysis problem (such as

segmentation) as an optimization problem with fidelity term specially designed for the local periodic structure of the crystal image [1, 23, 3].

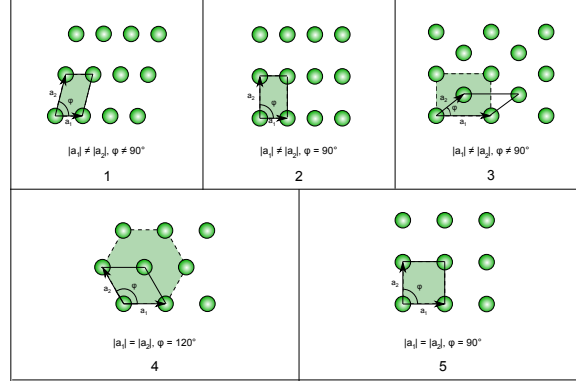


FIGURE 2. Five fundamental 2D Bravais lattices: 1 oblique, 2 rectangular, 3 centered rectangular (rhombic), 4 hexagonal, and 5 square. Black arrows represent lattice vectors in the Bravais lattices. Courtesy of Wikipedia.

Existing methods however often fall short for crystal image analysis with a variety of crystal patterns, fine features, and complicated geometry (see Figure 1 for examples). For instance, when the out-of-focus problem occurs, usually in optical microscopies and bright-field microscopies, the image intensity at the centers of atoms might vary a lot over the imaging domain, making it difficult to determine the reference configuration for atoms (see Figure 3 (left) for an example).

In this paper, we propose a two step procedure for crystal image analysis in these challenging scenarios. In the first step, an efficient phase-space sketching method is used to classify complicated crystal configurations and determine reference crystal patterns. In the second step, once the reference crystal patterns are learned from the first step, a recently developed crystal image analysis method based on two-dimensional synchrosqueezed transforms [30, 13] is applied to identify dislocations, cracks, grain boundaries, crystal orientation, deformation, and possibly other useful information.

A major difficulty of crystal pattern classification comes from the considerable variability within object classes and the inability of existing distances to measure image similarities. Part of this variability is due to grain orientation, crystal deformation, and defects; another part results from the imaging variation, e.g., the difference of image illumination, light reflection, and out-of-focus issues. An ideal transformation for classification should provide a representation invariant to such uninformative variability. Note that a representation that is completely invariant with respect to deformation would not distinguish different Bravais lattices (see Figure 2), since the lattices are equivalent up to affine transforms. The crystal image representation must therefore be capable of distinguishing different lattices, while being invariant to small elastic deformation due to external forces on grains.

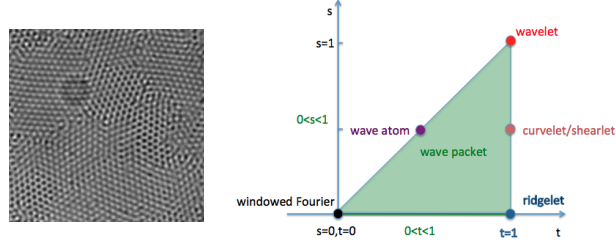


FIGURE 3. Left: An example of crystal images with the out-of-focus problem, in which an atom might be a black or a white dot in the crystal image. It is difficult to determine the position of atoms in this case. Courtesy of Yilong Han of Hong Kong University of Science and Technology. Right: The relation of windowed Fourier transform, wavelet transform, curvelet/shearlet transform, ridgelet transform, wave atom transform, and the wave packet transform in [31, 32].

Texture classification has been extensively studied in the literature. Translation and rotation invariant representations have been standard tools: these representations can be constructed with autoregression methods [9], hidden Markov models [27], local binary patterns [4], Gabor or wavelet transform modulus with rotation invariant features [5]. Scale and affine invariance has been also studied recently using affine adaption [11], fractal analysis [28], advanced learning [26], and combination of filters [33]. More recently, deep convolution networks [14] together with advanced learning techniques [2] have been applied to design deformation invariant representations [20].

The phase-space sketching proposed in this paper is an alternative method for the invariant texture classification based on the two-dimensional synchrosqueezed transform [31, 32]. The phase-space sketching encodes microscopic crystal images in a translation, rotation, illumination, and scale invariant representation. This new representation is stable to deformation and invariant to a class of elastic deformation in materials. The extent of the elastic deformation invariance is specified by user-defined parameters. As we shall see later, the results of the two-dimensional synchrosqueezed transforms can be applied to identify dislocations, cracks, grain boundaries, crystal orientation and deformation following the algorithms in [30, 13]. The proposed phase-space sketching only adds minimal computational cost to our existing methodologies for atomic resolution crystal image analysis.

The rest of this paper is organized as follows. We start by introducing the mathematical model of atomic resolution crystal images and our previous analysis framework on crystal image analysis in Section 2. In Section 3, we propose the phase space sketching based on the two-dimensional synchrosqueezed transform to identify reference crystal patterns. With the reference crystal patterns ready, a complete algorithm for invariant texture classification and segmentation is introduced. We

apply the whole algorithm to several real examples in materials science in Section 4. Finally, we present a brief summary of the proposed methodology in Section 5.

2. CRYSTAL IMAGE MODELING AND SYNCHROSQUEEZED TRANSFORM (SST)

2.1. Mathematical models for atomic resolution crystal image. Consider an atomic resolution $2D$ image (experimentally, this is often done for a thin slice of a $3D$ polycrystalline material) that may consist of multiple grains with the same Bravais lattice. Denote the reference Bravais lattice as

$$\mathcal{L} = \{av_1 + bv_2 : a, b \text{ integers}\},$$

where $v_1, v_2 \in \mathbb{R}^2$ represent two fixed lattice vectors (see Figure 2 for examples). Let $s(2\pi x)$ be the shape function describing a single perfect unit cell in the image, extended periodically in x with respect to the reference crystal lattice. We denote by Ω_k , $k = 1, \dots, M$, the grains the system consists of, and by $\Omega = \cup \Omega_k$ the domain occupied by the whole image. Hence, the polycrystal image $f : \Omega \rightarrow \mathbb{R}$ can be modeled as

$$(1) \quad f(x) = \sum_{k=1}^M \chi_{\Omega_k}(x) (\alpha_k(x) s(2\pi N \phi_k(x)) + c_k(x)),$$

where N is the reciprocal lattice parameter (or rather the relative reciprocal lattice parameter since the dimension of the image is normalized in our analysis). The crystal image model above works for both simple lattices (Bravais lattices listed in Figure 2) and complex lattices (such that the unit cell consists more than one atoms); extensions to more complicated images will be considered below. Here χ_{Ω_k} is the indicator function of each grain Ω_k ; $\phi_k : \Omega_k \rightarrow \mathbb{R}^2$ maps the atoms of grain Ω_k back to the configuration of a perfect crystal, i.e., it can be understood as the inverse of the elastic deformation. The local inverse deformation gradient is then given by $\nabla \phi_k$ in each Ω_k . The smooth amplitude envelope $\alpha_k(x)$ and the smooth trend function $c_k(x)$ in (1) model possible variation of intensity, illumination, etc. during the imaging process. By the $2D$ Fourier series \widehat{s} of s , we can rewrite (1) as

$$(2) \quad f(x) = \sum_{k=1}^M \chi_{\Omega_k}(x) \left(\sum_{\xi \in \mathcal{L}^*} \alpha_k(x) \widehat{s}(\xi) e^{2\pi i N \xi \cdot \phi_k(x)} + c_k(x) \right),$$

where \mathcal{L}^* is the reciprocal lattice of \mathcal{L} (recall that the shape function s is periodic with respect to the lattice \mathcal{L}).

2.2. Synchrosqueezed transform (SST). As shown in [30, 13], the $2D$ SST is an efficient tool to estimate the defect region and also the local inverse deformation gradient $G_0(x) = \sum_k \chi_{\Omega_k}(x) N \nabla \phi_k(x)$ in the interior of each grain Ω_k . The main observation is that, in each grain Ω_k , the image is a superposition of planewave-like components $\alpha_k(x) \widehat{s}(\xi) e^{2\pi i N \xi \cdot \phi_k(x)}$ with local wave vectors $N \nabla(\xi \cdot \phi_k(x))$. It has been shown in [31, 32] that the SST is able to estimate the local wave vectors accurately. Based on the local wave vector estimation, we can compute the inverse deformation gradient G_0 via a least square method, see §2.3 below.

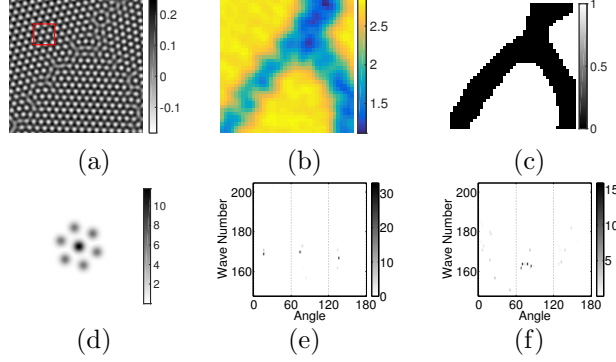


FIGURE 4. (a) An example of a crystal image. (b) The defect indicator $\text{mass}(x)$. (c) Identified defect region by thresholding $\text{mass}(x)$. (d) Windowed Fourier transform at a local patch indicated by a rectangle. (e) The SS energy distribution in polar coordinates at a point outside the defect region. (f) The SS energy distribution at a point in the defect region.

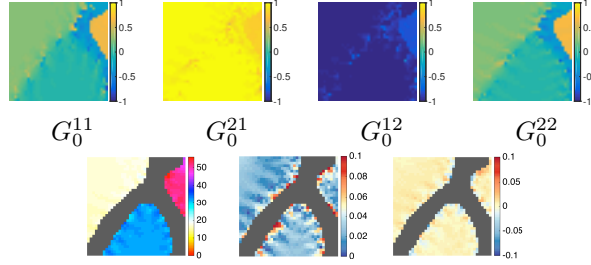


FIGURE 5. Top panel: Estimated inverse deformation gradient $G_0 \in \mathbb{R}^{2 \times 2}$ of the atomic resolution crystal image in Figure 4 (a). Bottom panel: The crystal orientation, the difference in principal stretches, and the volume distortion of G_0 . The grey mask in these figures is the defect region identified in Figure 4 (d).

The starting point of 2D SST is a wave packet $w_{a\theta x}$, which is, roughly speaking, constructed by translating, rotating, and rescaling or modulating a mother wave packet $w : \mathbb{R}^2 \rightarrow \mathbb{C}$ according to the spatial center parameter $x \in \mathbb{R}^2$, the angular parameter $\theta \in [0, 2\pi)$ in the frequency domain, and the radial parameter $a \in \mathbb{R}$ in the frequency domain [31, 32, 30, 13]. The wave packet transform coefficient of an image $f(x)$ at scale a and angle θ in the frequency domain, and at spatial location x is evaluated via $W_f(a, \theta, x) = \int_{\Omega} \overline{w_{a\theta x}}(y) f(y) dy$. The wave packet transform is a generalization of curvelet and wavelet transforms with better flexibility in frequency scaling and consequently is better suited to analyze crystal images with complicated geometry. There are two scaling parameters (t, s) in the wave packet transform. If $(t, s) = (1, 1)$, the wave packet transform is essentially the wavelet transform; if

$(t, s) = (1, 1/2)$, the wave packet transform becomes the curvelet transform (see Figure 3 (right) for an illustration). As a convolution with smooth wave packets, W_f is well-defined and smooth even under very low regularity requirements for f , e. g. $f \in L^\infty(\mathbb{R}^2)$.

In contrast to the windowed Fourier transform of a given crystal image, whose spectrum spreads out in the phase space as illustrated in Figure 4(d), the 2D synchrosqueezed transform (SST) based on wave packets aims at a sharpened phase-space representation. In the SST, for each (a, θ, x) , we define the corresponding local wave vector estimation

$$v_f(a, \theta, x) = \Re \frac{\nabla_x W_f(a, \theta, x)}{2\pi i W_f(a, \theta, x)}$$

for $|W_f(a, \theta, x)| > \gamma$, where γ is a threshold parameter to ensure stability of the estimation. Here, $\nabla_x W_f$ denotes the gradient of W_f with respect to its third argument x .

If $f(x)$ is a plane wave with a wave vector $(v_1, v_2) \in \mathbb{R}^2$, then simple algebraic calculation shows that the local wave vector estimation $v_f(a, \theta, x)$ is exactly (v_1, v_2) whenever $W_f(a, \theta, x)$ is not zero. When $f(x)$ is a superposition of planewaves with well-separated local wave vectors $\{(v_1^{(k)}, v_2^{(k)})\}_k$, by the stationary phase approximation, $v_f(a, \theta, x) \approx (v_1^{(k)}, v_2^{(k)})$ when $(a \cos \theta, a \sin \theta)$ is close to some local wave vector $(v_1^{(k)}, v_2^{(k)})$. In the case of crystal images, locally $f(x)$ is a superposition of deformed planewaves. By applying Taylor expansion to make approximations, one can also show that the local wave vector estimation $v_f(a, \theta, x)$ can still approximate the local wave vectors of $f(x)$ (see [30] for the detailed analysis). Even in the presence of heavy noise, this approximation is still reasonably good by applying the SST based on highly redundant wave packet frames [29].

Motivated by the property of the local wave vector estimation v_f , the synchrosqueezed (SS) energy distribution of f is constructed as

$$(3) \quad T_f(v, x) = \iint_{(a, \theta) \in D(x, \gamma)} |W_f(a, \theta, x)|^2 \delta(v_f(a, \theta, x) - v) a \, da \, d\theta,$$

where

$$D(x, \gamma) := \{(a, \theta) \in (0, \infty) \times (0, 2\pi) : |W_f(a, \theta, x)| > \gamma\}$$

and δ in (3) denotes the Dirac measure. The SST squeezes the wave packet spectrum $|W_f(a, \theta, x)|^2$ according to $v_f(a, \theta, x)$ to obtain a sharpened and concentrated representation of the image in the phase space. Hence, in the interior of a grain, the SS energy distribution T_f has a support concentrating around local wave vectors $N\nabla(\xi \cdot \phi_k(x))$, $\xi \in \mathcal{L}^*$, and is given approximately by (see e.g., Figure 4(e) in polar coordinate)

$$(4) \quad T_f(v, x) \approx \sum_{\xi \in \mathcal{L}^*} \alpha_k(x)^2 |\hat{s}(\xi)|^2 \delta(v - N\nabla(\xi \cdot \phi_k(x))),$$

understood in the distributional sense. Therefore, by locating the energy peaks of T_f , we can obtain estimates of local wave vectors $N\nabla(\xi \cdot \phi_k(x))$ and also their associated spectral energy. In practice, we choose high energy peaks corresponding

to ξ close to the origin in the reciprocal lattice to estimate the inverse deformation gradient G_0 and grain boundaries to guarantee numerical stability.

2.3. SST based crystal image analysis. In the case of a crystal image that consists of only one kind of lattice in the image, it has been shown in [30, 13] that the SST can be applied to estimate the inverse deformation gradient G_0 , grain boundaries, and defects. For simplicity, let us focus on the case of hexagonal lattices in this section. It is straightforward to generalize to other Bravais lattices.

In the case of hexagonal lattices, we have six dominant reciprocal lattice vectors $\xi \in \mathcal{L}^*$ such that $|\widehat{s}(\xi)|$ is significant, which can be further reduced to three due to the symmetry $\xi \leftrightarrow -\xi$. We will henceforth denote these as ξ_n , $n = 1, 2, 3$, and denote by $v_n^{\text{est}}(x)$ the estimate of $N\nabla(\xi_n \cdot \phi_k(x)) = N(\nabla\phi_k(x))\xi_n$. The inverse deformation gradient $G_0(x) = \nabla\phi_k(x)$ is determined by a least squares fitting to identify a linear transformation that maps the reference reciprocal lattice vectors $N\xi_n$ to the estimated local wave vectors v_n^{est} :

$$G_0(x) = \underset{G}{\operatorname{argmin}} \sum_{n=1}^3 |v_n^{\text{est}}(x) - NG\xi_n|^2.$$

In practice, for each physical point x we represent $T_f(\cdot, x)$ in polar coordinates $(r, \vartheta) \in [0, \infty) \times [0, \pi)$ (the information in $\vartheta \in [\pi, 2\pi)$ is redundant due to symmetry). To identify the peak locations $\{v_n^{\text{est}}\}$, we choose the grid point with highest amplitude in each $\pi/3$ -degree sector of ϑ .

Since the local wave vector estimation is no longer valid around the crystal defects, the SS energy distribution T_f does not have dominant energy peaks around local wave vectors. Hence, we may characterize the defect region by quantifying how concentrated the energy distribution is. One possible way is to use an indicator function as follows. For each $n \in \{1, 2, 3\}$ (corresponding to one of the sectors), we define

$$w_n(x) = \frac{\int_{B_\delta(v_n^{\text{est}})} T_f(v, x) dv}{\int_{\arg v \in [(n-1)\pi/3, n\pi/3)} T_f(v, b) dv},$$

where $B_\delta(v_n^{\text{est}})$ denotes a small ball around the estimated local wave vector v_n^{est} . Hence, $\text{mass}(x) := \sum_n w_n(x)$ will be close to 3 in the interior of a grain due to (4), while its value will be much smaller than 3 near the defects. This is illustrated in Figure 4(b), where we show $\text{mass}(x)$ for the crystal image in Figure 4(a). The estimate of defect regions can be obtained by a thresholding $\text{mass}(x)$ at some value $\eta \in (0, 3)$ according to

$$\Omega_d = \{x \in \Omega : \text{mass}(x) < \eta\},$$

an illustration of which is shown in Figure 4(c). Figure 5 shows the estimate of G_0 by the SST. When showing the result, we have used a more transparent way to represent the inverse deformation gradient G_0 via the polar decomposition $G_0(x) = U_0(x)P_0(x)$ for each point $x \in \Omega$, where $U_0(x)$ is a rotation matrix and $P_0(x)$ is a positive-semidefinite symmetric matrix. At each position x , the crystal orientation

can be estimated via the rotation angle of $U_0(x)$; the volume distortion of $G_0(x)$ can be visualized by $\det(G_0(x)) - 1$; the quantity $|\lambda_1(x) - \lambda_2(x)|$ characterizes the difference in the principal stretches of $G_0(x)$ as a measure of shear strength, where $\lambda_1(x)$ and $\lambda_2(x)$ are the eigenvalues of $P_0(x)$. The bottom panel of Figure 5 shows these quantities corresponding to the estimate of G_0 in the top panel. In later numerical examples, we will always present the estimated inverse deformation gradient in the same fashion.

3. PHASE SPACE SKETCHING

To extend the crystal image analysis to more complicated scenario, in this section, we propose the phase-space sketching, which is a sparse invariant representation of the phase-space information obtained by synchrosqueezed transforms. The phase-space sketching will enable classification of different crystal types presented in the same image or across images.

3.1. Invariant representation. As compared to the crystal image model with a unique Bravais lattice in the previous section, the mathematical model of a crystal image that consists of multiple types of lattices can be written as

$$\begin{aligned}
 (5) \quad f(x) &= \sum_{k=1}^M \chi_{\Omega_k}(x) (\alpha_k(x) s_k(2\pi N \phi_k(x)) + c_k(x)) \\
 &= \sum_{k=1}^M \chi_{\Omega_k}(x) \left(\sum_{\xi \in \mathcal{L}_k^*} \alpha_k(x) \widehat{s}_k(\xi) e^{2\pi i N \xi \cdot \phi_k(x)} + c_k(x) \right).
 \end{aligned}$$

The image classification and segmentation problem is to identify each domain Ω_k and classify its corresponding shape function s_k . The main difficulty is due to the considerable variability within object classes (e.g., grain orientation, crystal deformation, defects, and difference of image illumination). Our goal is to design a representation of the crystal image that is invariant to most of these variability.

It has been shown in [12, 2] that, deep convolution networks have the ability to build large-scale invariants stable to deformations. Combined with advanced learning techniques, the convolution network like the scattering transform can provide deformation invariance [20] and could be used for the problem discussed in this paper. On the other hand, since our problem is more specific than general image classification, we aim to design a more efficient and specific method. Taking advantage of the periodic structure of crystal images, we introduce the phase-space sketching instead of applying the convolution network for the purpose of computational efficiency. The phase-space sketching is a nonlinear operator rescaling, shifting, and coarsening the SS energy distribution.

Let us recall the definition of the SS energy distribution in Equation (3), written in polar coordinate as

$$T_f(r, \vartheta, x) = \iint_{(a, \theta) \in D(x, \gamma)} |W_f(a, \theta, x)|^2 \delta(v_f(a, \theta, x) - (r \cos \vartheta, r \sin \vartheta)) a \, da \, d\theta,$$

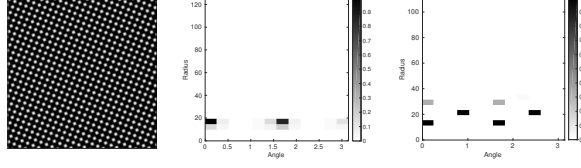


FIGURE 6. Left: an example of atomic resolution crystal images $f(x) = \alpha(x)s(2\pi N\phi(x))$. Middle: the phase-space sketch $\tilde{S}(T_f^s, h, u)(r, \vartheta, x)$ by the polar windowed Fourier transform for a fixed x (by a similar strategy of sketching applying on energy distribution of the polar windowed Fourier transform). Right: the phase-space sketch $\tilde{S}(T_f^s, h, u)(r, \vartheta, x)$ by the SST at the same point x . The sketch by the SST is cleaner and provides multi points in the reciprocal lattice \mathcal{L}^* of the Bravais lattice \mathcal{L} of the shape function $s(x)$.

for $(r, \vartheta) \in [0, \infty) \times [0, \pi)$. Note that the SS energy distribution is translation invariant because the modulus of the wave packet coefficient $|W_f(a, \theta, x)|$ is invariant to the translation of the image $f(x)$. A simple idea to achieve the rotation invariance might be shifting $T_f(r, \vartheta, x)$ in the variable ϑ such that $T_f(r, \vartheta, x)$ always takes its maximum value at a specific location. However, this shifting procedure is usually sensitive to the crystal deformation. This motivates the following shifting and coarsening process to reduce the influence of rotation and deformation simultaneously. For a step size $h \in (0, \pi)$ in the angle coordinate ϑ and a step size $u > 0$ in the radial coordinate r , we define the phase-space sketch via a coarsening procedure as follows.

Let

$$(r_0(x), \theta_0(x)) = \arg \max_{r \in [0, \infty), \theta \in [0, \pi)} T_f(r, \vartheta, x),$$

we defined the shifted and rescaled SS energy distribution with a scaling parameter \mathbf{s} as

$$T_f^s(r, \vartheta, x) = T_f\left(\frac{r_0(x)r}{\mathbf{s} + u/2}, \vartheta + \theta_0(x) - \frac{h}{2}, x\right).$$

Then the phase-space sketch of the new SS energy distribution $T_f^s(r, \vartheta, x)$ is defined as a local average of the shifted and rescaled SS energy distribution

$$(6) \quad \tilde{S}(T_f^s, h, u)(r, \vartheta, x) = \int_{\lfloor \frac{\vartheta}{h} \rfloor h}^{\lfloor \frac{\vartheta}{h} \rfloor h + h} \int_{\lfloor \frac{r}{u} \rfloor u}^{\lfloor \frac{r}{u} \rfloor u + u} T_f^s(\tilde{r}, \tilde{\vartheta}, x) \tilde{r} d\tilde{r} d\tilde{\vartheta}$$

for $(r, \vartheta) \in [0, \infty) \times [0, \pi)$, where $\lfloor \cdot \rfloor$ means the floor operator.

This operation can be understood as a binning operator that collects varying local wave vectors into fixed bins in the phase space, and hence reduces the influence of the deformation. Overall, the phase-space sketching is a nonlinear transform (with respect to the image f) that squeezes the phase-space energy distribution via synchrosqueezing and coarsening into the sketch $\tilde{S}(T_f, h, u)$, resulting in a representation invariant to small deformation.



FIGURE 7. A separable invariant along rotations and translations cannot distinguish the left and right texture patterns, but a joint rotation-translation invariant can [20]. Courtesy of Sifre et al..

The extend of the deformation invariance of $S(T_f^s, h, u)$ is determined by the step sizes h and u . Note that a fully deformation invariant representation would not be able to distinguish different Bravais lattices (see Figure 2), since these lattices are the same in the quotient group of affine transforms. Hence, we should choose appropriate step sizes h and u such that: 1) they are sufficiently large, making $S(T_f^s, h, u)$ invariant to small elastic deformation due to external forces on the material; 2) they are small enough such that $S(T_f^s, h, u)$ is capable of distinguishing different lattices.

The sketch $\tilde{S}(T_f^s, h, u)$ is also invariant to rotation and scaling. After shifting and rescaling, for a fixed x , the new SS energy distribution $T_f^s(r, \vartheta, x)$ reaches its maximum value at $(s + \frac{u}{2}, \frac{h}{2})$. Hence, the sketch $\tilde{S}(T_f^s, h, u)(r, \vartheta, x)$ has the maximum value in $[s, s + u) \times [0, h)$ for each fixed x .

It is worth pointing out that the sketch $\tilde{S}(T_f^s, h, u)(r, \vartheta, x)$ is separably invariant with respect to rotation and translation. Therefore, the sketch cannot discriminate a class of similar texture patterns, e.g. see Figure 7 for an example of two images sharing similar absolute values of the wave packet coefficients. Fortunately, this is not a problem in atomic resolution crystal image analysis, since all crystal patterns behave similarly to the pattern in Figure 7 (left).

Finally, to remove the influence of the amplitude function $\alpha(x)$, i.e., obtaining the illumination invariance, we normalize the magnitude of the phase-space sketch $\tilde{S}(T_f^s, h, u)(r, \vartheta, x)$ and define

$$S(T_f^s, h, u)(r, \vartheta, x) = \frac{\tilde{S}(T_f^s, h, u)(r, \vartheta, x)}{\max_{r \in [0, \infty), \theta \in [0, \pi)} \tilde{S}(T_f^s, h, u)(r, \vartheta, x)}.$$

One may also consider sketching other more standard phase-space representations, e.g., the polar windowed Fourier transform or wavelet transform. However, it is more advantageous to combine sketching with the synchrosqueezed transforms. As we have shown in Figure 4, the SS energy distribution has concentrated support around the local wave vectors of the crystal image, while the results of windowed Fourier transform or wavelet transform are more spread-out. Hence, the sketch of the windowed Fourier or wavelet transform is not as clean as that of the SS energy distribution (see the comparison in Figure 6). Moreover, the SS energy distribution provides useful information for crystal image analysis and computing its sketching only adds minimal computational overhead.

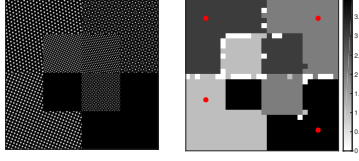


FIGURE 8. Left: a toy example of atomic resolution crystal images with different crystal patterns. Right: classification results of the sketch by the SST. The crystal image is of size 512×512 . We sub-sample the crystal image to save computation (one sample every 4 pixels) and generate local patches of size 65×65 pixels centered at the sub-sampled points. Each patch is associated with a phase-space sketch. These patches are classified based on the compressed feature vector of the sketch using spectral clustering. The centers of outlier patches are indexed with zeros.

3.2. Classification. We may apply the phase-space sketch to classify crystal textures in a complicated crystal image. Although advanced classifiers such as SVM are useful tools for classification, here we present some simple and efficient classification methods.

As we have seen in Figure 6, the phase-space sketch $S(T_f^s, h, u)$ at a point x in the interior of a grain has well-separated supports indicating the reciprocal lattice \mathcal{L}^* of the Bravais lattice \mathcal{L} of the crystal pattern. Hence, the locations and the magnitudes of the supports are important features for crystal pattern classification. In the case of a complicated crystal image, if two grains share the same crystal pattern, they should have the same phase-space sketch $S(T_f^s, h, u)$ at the locations x sufficiently far away from grain boundaries. Therefore, we only need to identify major groups of the sketch $S(T_f^s, h, u)$ at different x 's and choose a representative sketch from each major group. Other sketch outliers are due to the influence of grain boundaries on the phase-space representation; each sketch outlier contains the information of at least two crystal patterns and looks like a superposition of more than one sketches.

A simple idea for classification is to define an appropriate distance to measure the similarity of different phase-space sketches and apply the spectral clustering to identify the major groups of the sketches. Since the types of crystal textures are limited, it is not necessary to use the whole sketch for discrimination. To ensure that the method is as efficient as possible, features contained in the sketch invariant to uninformative variability in crystal images are more important. Observe that the phase-space sketch is able to sketch out the multi-scale reciprocal lattice \mathcal{L}^* (see Figure 6 (right)), and the numbers of supports at different scales largely determine the crystal pattern. It is sufficient to use these numbers as a compressed feature vector to represent the sketch. For example, the feature vector of the sketch in Figure 6 (right) is $(2, 2, 2)$, where each 2 means that there are 2 supports at each scale. Note that the number of supports are invariant to translation, rotation, illumination, and small deformation. Hence, the feature vector by the number of

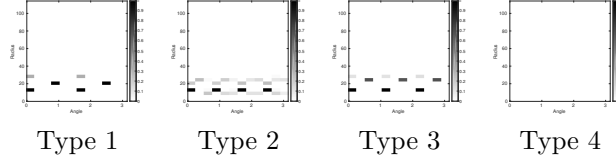


FIGURE 9. From left to right, the phase-space sketch $S(T_f^s, h, u)(r, \vartheta, x)$ of the SST corresponding to the type of reference configuration identified in Figure 8. Red dots in Figure 8 (right) indicate the position x 's of the sketches in this figure.

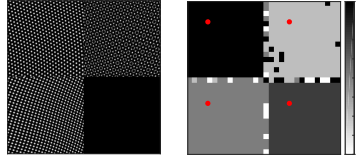


FIGURE 10. Left: a toy example of atomic resolution crystal images with different crystal patterns. Right: classification results by the sketch of the SST. Numerical results were obtained using the same setting as in Figure 8.

supports in sketches is a compressed invariant representation of crystal patterns. The standard Euclidean distance of vectors is a natural choice to measure the similarity of these compressed invariant representations. Using the number of supports only might be too ambitious in some cases. A better way is to take advantage of the magnitudes of the peaks in these supports, once two crystal patterns have sketches sharing the same numbers of supports. For example, a simple idea is to set up a threshold parameter and only count the number of supports above this threshold. In practice, this simple idea is sufficient to discriminate most crystal patterns in real applications.

Finally, we provide several synthetic examples to demonstrate the efficiency of the proposed compressed feature vector for classification. The first example in Figure 8 (left) contains three different crystal patterns and one vacancy area, and each pattern has two grains with different orientations and scales. The SST is applied to generate the phase-space sketch and the corresponding compressed feature vectors at each pixel of the crystal image. The spectral clustering algorithm is able to identify four major groups of compressed feature vectors. According to the clustering results of the feature vectors, we group the corresponding pixels together and visualize the results in Figure 9 (right).

The third example in Figure 10 (left) is similar to the first example but the crystal image has been smoothly deformed. As shown in Figure 10 (right) and Figure 11, the proposed method succeeds to detect all crystal patterns and their sketches.

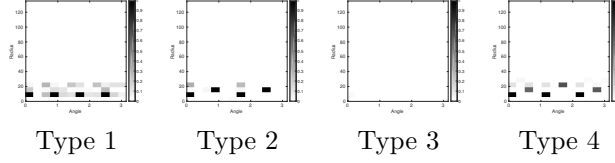


FIGURE 11. From left to right, the phase-space sketch $S(T_f^s, h, u)(r, \vartheta, x)$ of the SST corresponding to the type of reference configuration identified in Figure 10. Red dots in Figure 10 (right) indicate the position x 's of the sketches in this figure.

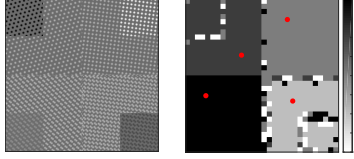


FIGURE 12. Left: a toy example of atomic resolution crystal images with different crystal patterns. Right: classification results by the sketch of the SST. Numerical results were obtained using the same setting as in Figure 8.

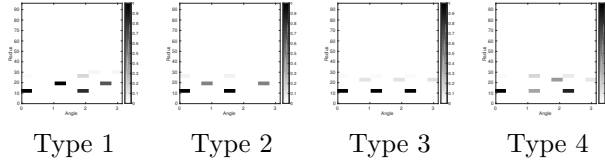


FIGURE 13. From left to right, the phase-space sketch $S(T_f^s, h, u)(r, \vartheta, x)$ of the SST corresponding to the type of reference configuration identified in Figure 12. Red dots in Figure 12 (right) indicate the position x 's of the sketches in this figure.

In the last example in Figure 12 (left), there are four different crystal patterns (two kinds of square lattices and two kinds of hexagonal lattices) with different levels of illumination. As shown in Figure 12 (right) and Figure 13, the proposed method is able to detect all crystal patterns and their sketches. This is a very challenging example. As we can see in the sketches in Figure 13, Type 1 and 2 sketches almost share the same support (and so do Type 3 and 4). Hence, as discussed previously, only the number of supports with peaks over an appropriate threshold is used in constructing the compressed feature vector.

3.3. Segmentation. In the previous section, we have applied the phase-space sketching to identify reference sketches for different crystal patterns in a complicated crystal image. As shown in Figure 8 to 12, a crystal image can be roughly

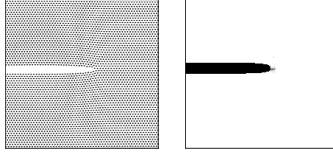


FIGURE 14. The atomic simulation at zero temperature to examine dislocation emission from a crack tip.

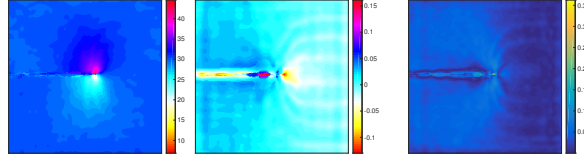


FIGURE 15. Numerical results of the example in Figure 14. Left: crystal orientation. Middle: the volume distortion of the elastic deformation. Right: the difference in principle stretches of the elastic deformation.

partitioned into several pieces and each piece contains grains sharing the same crystal pattern. However, we are not able to determine an accurate partition due to sketch outliers at grain boundaries. Since we already have the reference sketches by the algorithm in the previous section, we can simply match the sketch outliers with the reference sketches and identify the most possible type of crystal pattern. Once we have completed the image segmentation for different crystal patterns, the atomic resolution crystal image analysis in Section 2 is applied within each type of crystal patterns to estimate defects and crystal deformations. This completes the complicated crystal image analysis.

4. QUANTITATIVE ANALYSIS IN REAL APPLICATIONS

This section presents several real examples in materials science to demonstrate the efficiency of the proposed method in this paper. These atomic crystal examples include crack propagation, phase transition, and self-assembly.

4.1. Crack propagation. Accurate and quantitative estimation of the elastic deformation in the presence of plastic deformation and defects (cracks and dislocations) is crucial for predicting a critical loading state that results in crack growth and dislocation motion, understanding the dislocation nucleation/emission from an originally pristine crack tip, quantifying the effect that pre-existing dislocations surrounding a crack tip can have on its driving force, and exploring how the cracktip shape impacts the dislocation emission process [34], just to name a few.

Figure 14 (left) is an example of the atomic simulation at zero temperature to examine dislocation emission from a crack tip. We apply the proposed algorithms in this paper to identify the crystal pattern, the crack region, and estimate the elastic

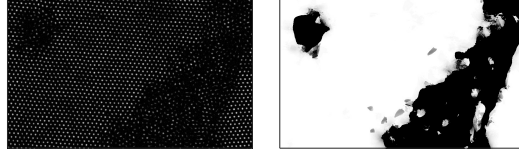


FIGURE 16. Left: melting behavior of thin crystalline films [18]. Courtesy of Yilong Han of Hong Kong University of Science and Technology, and Arjun Yodh of Pennsylvania State University [16]. Right: defect and liquid regions are indicated in black, while solid crystal regions and grain islands are in white.

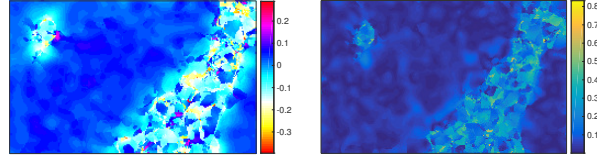


FIGURE 17. Deformation analysis of the example in Figure 16 (left). Left: the volume distortion of the elastic deformation. Right: the difference in principle stretches of the elastic deformation.

deformation of this example. As shown in Figure 14 (right), the crack estimation is accurate up to an error less than one atom. Figure 15 shows the estimation of the crystal orientation, the volume distortion and the difference in principle stretches of the elastic deformation. These results quantitatively show the interaction between the crack and the perfect crystal region through elastic deformation, especially around the crack-tip and in the direction of the crack propagation.

4.2. Phase transition. With the development of digital video microscopy [16, 18, 17], researchers are able to observe the phase transition (between solid, liquid and gaseous states of matter) with single particle resolution. The behavior of important quantities at the atomic scale (e.g., defects, deformation, phase interfaces) presents interesting new questions and challenges for both theory and experiment in materials science. Research in this direction is limited by the difficulty of imaging and analyzing atomic crystals. In the aspect of data analysis, the challenge comes from the fact that it is difficult to track the atoms in the evolution process of phase transition, especially in the case of irregular patterns (e.g. liquid or gas states). The proposed algorithm in this paper is free of tracking atoms, offering a new means to examine fundamental questions in phase transition.

4.2.1. Solid-liquid phase transition. Crystal melting (solid-liquid phase transition) is of considerable importance, but our understanding of the melting process in the atomic scale is far from complete. In particular, the kinetics of this phase transition have proved difficult to predict [10]. Scientists have been trying to verify

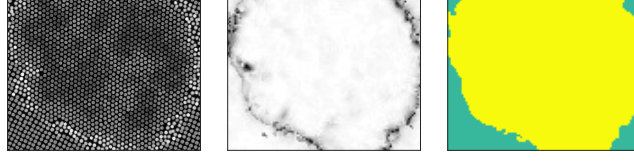


FIGURE 18. Left: a microscopic image showing the simulation of nucleation mechanism in solid-solid phase transitions [17]. Courtesy of Yilong Han of Hong Kong University of Science and Technology, and Arjun Yodh of Pennsylvania State University. Middle: defects and interfaces are visualized in black. Right: identified hexagonal lattice in yellow and square lattice in green.

old conjectures and establish new theories in describing the crystal melting process at the atomic scale [16, 18].

Figure 16 shows an example of thin crystalline films during the melting process [18]. We apply the proposed algorithms in this paper to identify the solid and liquid regions, and estimate the elastic deformation of this example. As shown in Figure 16 (right), the estimation of the interfaces between solid and liquid states are in line with the image in Figure 16 (left) by visual inspection. This result also matches the fact that capillary waves roughen the solid-liquid surface, but locally the intrinsic interface is sharply defined [7]. Figure 17 shows the estimation of the crystal orientation, the volume distortion and the difference in principle stretches of the elastic deformation (only the results in the solid part are informative). These results quantitatively show the interaction between the solid and liquid parts. The elastic deformation of the solid crystal structure near the solid-liquid interfaces has a larger strain.

4.2.2. Solid-solid phase transition. It is well known that different geometric arrangements of the same atom or crystal phase can produce materials with different properties. Solid-solid phase transitions can significantly change the physical properties of crystalline solids. A spectacular example of this effect is coal and diamond. Scientists have been trying to identify the right circumstances under which the phase transition occurs, to understand the mechanisms that facilitate phase transitions, and to control the transition process [17].

Figure 18 (top-left) shows the simulation of nucleation mechanism in solid-solid phase transitions [17]. In this example, we focus on identifying different crystal patterns for the sake of shortening the manuscript. We apply the proposed algorithms in this paper to identify two solid crystal patterns, and defects. As shown in Figure 18 (right two figures), the estimation of the interface between two different solid crystal patterns agrees with the image in Figure 18 (top-left) by visual inspection.

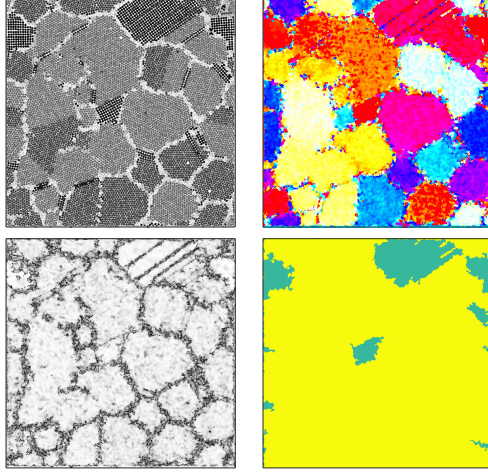


FIGURE 19. Top-left: an example of the crystallization dynamics of sedimenting hard spheres in large systems [15]. Courtesy of Marjolein Dijkstra at Utrecht University. Top-right: different colors encode different crystal orientations. Bottom-left: identified defects in black. Bottom-right: identified square crystal lattice in green and hexagonal crystal lattice in yellow.

4.2.3. Self-assembly. A disordered system of pre-existing components can form an organized structure or pattern through local interactions among the components themselves without external direction. This evolution process is called self-assembly. Self-assembly is an attractive approach for fabricating complex synthetic structures with specific functions [6]. The most common approach to design a self-assembly strategy is by trial and error, where various synthesis methods are studied. To discover new self-assembly strategies to make artificial materials with desired mechanical and biological properties, it is crucial to understand the detailed dynamics of formation in self-assembly.

Figure 19 shows the final configuration of the crystallization dynamics of sedimenting hard spheres [15]. The crystallization process is a purely entropy-driven phase transition from a disordered fluid phase to face-centered-cubic crystal structures and hexagonal-close-packed structures. We apply the proposed method in this paper to analyze the crystal image in Figure 19 (top-left). Numerical results of crystal orientations, defects, and types of crystal patterns are visualized in Figure 19 top-right, bottom-left, and bottom right, respectively.

4.3. Out-of-focus issue. In the last numerical example, we test the proposed crystal analysis method on an image with the out-of-focus problem, where it is difficult to determine the positions of atoms and even gain boundaries by visual inspection (see Figure 20 (left) for examples). Some structured noise in form of dark disks also increases the difficulty of image analysis. We apply the proposed method in this paper to analyze the example in Figure 19 (left), show the defect estimation

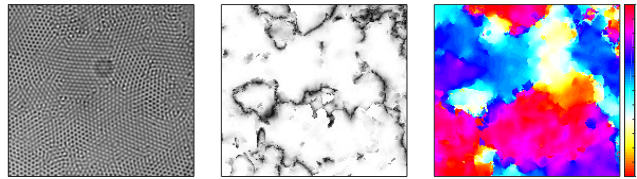


FIGURE 20. Left: an example of atomic resolution crystal images with the out-of-focus problem. Courtesy of Yilong Han of Hong Kong University of Science and Technology. Middle: identified defects. Right: crystal orientation estimation.

in the middle of Figure 20, and visualize the crystal orientation estimation in right panel of Figure 20. Numerical results show that the proposed method is stable to the out-of-focus problem and the structured noise.

5. CONCLUSION

We propose a tool set for automatic and quantitative characterization of complex microscopic crystal images based on the phase-space sketching and synchrosqueezed transforms. This method encodes microscopic crystal images into a translation, rotation, illumination, scale, and small deformation invariant representation. We have applied this method to analyze various atomic resolution crystal images in materials science, e.g., crack propagation images, phase transition images, self-assembly images. Let us mention two possible future directions: 1) it is worth exploring other advanced image segmentation algorithms to improve the performance of the proposed method at grain boundaries; 2) it is useful to extend the current framework for three-dimensional atomic resolution crystal image analysis.

REFERENCES

- [1] B. Berkels, A. Rätz, M. Rumpf, and A. Voigt. Extracting grain boundaries and macroscopic deformations from images on atomic scale. *J. Sci. Comput.*, 35:1–23, 2008.
- [2] J. Bruna and S. Mallat. Invariant scattering convolution networks. *IEEE Transactions on Pattern Analysis and Machine Intelligence*, 35(8):1872–1886, Aug 2013.
- [3] M. Elsey and B. Wirth. Fast automated detection of crystal distortion and crystal defects in polycrystal images. *Multi. Model. Simul.*, 12:1–24, 2014.
- [4] Z. Guo, L. Zhang, and D. Zhang. Rotation invariant texture classification using {LBP} variance (lbvp) with global matching. *Pattern Recognition*, 43(3):706 – 719, 2010.
- [5] G. M. Haley and B. S. Manjunath. Rotation-invariant texture classification using a complete space-frequency model. *IEEE Transactions on Image Processing*, 8(2):255–269, Feb 1999.
- [6] B. Hatton, L. Mishchenko, S. Davis, K. H. Sandhage, and J. Aizenberg. Assembly of large-area, highly ordered, crack-free inverse opal films. *Proceedings of the National Academy of Sciences*, 107(23):10354–10359, 2010.
- [7] J. Hernández-Guzmán and E. R. Weeks. The equilibrium intrinsic crystal–liquid interface of colloids. *Proceedings of the National Academy of Sciences*, 106(36):15198–15202, 2009.
- [8] J. J. Juarez, P. P. Mathai, J. A. Liddle, and M. A. Bevan. Multiple electrokinetic actuators for feedback control of colloidal crystal size. *Lab Chip*, 12:4063–4070, 2012.

- [9] R. L. Kashyap and A. Khotanzad. A model-based method for rotation invariant texture classification. *IEEE Transactions on Pattern Analysis and Machine Intelligence*, PAMI-8(4):472–481, July 1986.
- [10] A. Laaksonen, V. Talanquer, and D. W. Oxtoby. Nucleation: Measurements, theory, and atmospheric applications. *Annual Review of Physical Chemistry*, 46(1):489–524, 1995. PMID: 24341941.
- [11] S. Lazebnik, C. Schmid, and J. Ponce. A sparse texture representation using local affine regions. *IEEE Trans. Pattern Anal. Mach. Intell.*, 27(8):1265–1278, Aug. 2005.
- [12] Y. LeCun, K. Kavukcuoglu, and C. Farabet. *Convolutional networks and applications in vision*, pages 253–256. 2010.
- [13] J. Lu, B. Wirth, and H. Yang. Combining 2D synchrosqueezed wave packet transform with optimization for crystal image analysis. *Journal of the Mechanics and Physics of Solids*, pages –, 2016.
- [14] S. Mallat. Group invariant scattering. *Communications on Pure and Applied Mathematics*, 65(10):1331–1398, 2012.
- [15] M. Marechal, M. Hermes, and M. Dijkstra. Stacking in sediments of colloidal hard spheres. *The Journal of Chemical Physics*, 135(3), 2011.
- [16] P. Pàmies. Defect-less melting. *Nature Materials*, 11(910), 2012.
- [17] Y. Peng, F. Wang, Z. Wang, A. M. Alsayed, Z. Zhang, A. G. Yodh, and Y. Han. Two-step nucleation mechanism in solidsolid phase transitions. *Nature Materials*, advance online publication, Sept. 2014.
- [18] Y. Peng, Z. Wang, A. M. Alsayed, A. G. Yodh, and Y. Han. Melting of colloidal crystal films. *Phys. Rev. Lett.*, 104:205703, May 2010.
- [19] Y. Shibuta, K. Oguchi, T. Takaki, and M. Ohno. Homogeneous nucleation and microstructure evolution in million-atom molecular dynamics simulation. *Scientific Reports*, 5(13534), 2015/08/27/online.
- [20] L. Sifre and S. Mallat. Rotation, scaling and deformation invariant scattering for texture discrimination. In *2013 IEEE Conference on Computer Vision and Pattern Recognition*, pages 1233–1240, June 2013.
- [21] H. M. Singer and I. Singer. Analysis and visualization of multiply oriented lattice structures by a two-dimensional continuous wavelet transform. *Phys. Rev. E*, 74:031103, 2006.
- [22] G. Stone, C. Ophus, T. Birol, J. Ciston, C.-H. Lee, K. Wang, C. J. Fennie, D. G. Schlom, N. Alem, and V. Gopalan. Atomic scale imaging of competing polar states in a ruddlesden-popper layered oxide. *Nature Communications*, 7, 2016.
- [23] E. Strekalovskiy and D. Cremers. Total variation for cyclic structures: Convex relaxation and efficient minimization. In *Computer Vision and Pattern Recognition (CVPR), 2011 IEEE Conference on*, pages 1905–1911, 2011.
- [24] A. Stukowski and K. Albe. Extracting dislocations and non-dislocation crystal defects from atomistic simulation data. *Model. Simul. Mater. Sci. Eng.*, 18:085001, 2010.
- [25] B. Unal, V. Fournée, K. J. Schnitzenbaumer, C. Ghosh, C. J. Jenks, A. R. Ross, T. A. Lograsso, J. W. Evans, and P. A. Thiel. Nucleation and growth of ag islands on fivefold al-pd-mn quasicrystal surfaces: Dependence of island density on temperature and flux. *Phys. Rev. B*, 75:064205, Feb 2007.
- [26] M. Varma and A. Zisserman. Classifying images of materials: Achieving viewpoint and illumination independence. In *Proceedings of the 7th European Conference on Computer Vision-Part III, ECCV '02*, pages 255–271, London, UK, UK, 2002. Springer-Verlag.
- [27] W.-R. Wu and S.-C. Wei. Rotation and gray-scale transform-invariant texture classification using spiral resampling, subband decomposition, and hidden markov model. *IEEE Transactions on Image Processing*, 5(10):1423–1434, Oct 1996.
- [28] Y. Xu, H. Ji, and C. Fermuller. A projective invariant for textures. In *Proceedings of the 2006 IEEE Computer Society Conference on Computer Vision and Pattern Recognition - Volume 2, CVPR '06*, pages 1932–1939, Washington, DC, USA, 2006. IEEE Computer Society.

- [29] H. Yang. Statistical analysis of synchrosqueezed transforms. *Applied and Computational Harmonic Analysis*, 2017.
- [30] H. Yang, J. Lu, and L. Ying. Crystal image analysis using 2d synchrosqueezed transforms. *Multiscale Modeling & Simulation*, 13(4):1542–1572, 2015.
- [31] H. Yang and L. Ying. Synchrosqueezed wave packet transform for 2D mode decomposition. *SIAM J. Imaging Sci.*, 6:1979–2009, 2013.
- [32] H. Yang and L. Ying. Synchrosqueezed curvelet transform for two-dimensional mode decomposition. *SIAM J. Math. Anal.*, 46(3):2052–2083, 2014.
- [33] J. Zhang and T. Tan. Affine invariant classification and retrieval of texture images. *Pattern Recognition*, 36(3):657 – 664, 2003.
- [34] J. A. Zimmerman and R. E. Jones. The application of an atomistic j -integral to a ductile crack. *Journal of Physics: Condensed Matter*, 25(15):155402, 2013.

DEPARTMENT OF MATHEMATICS, DUKE UNIVERSITY, BOX 90320, DURHAM NC 27708, USA
E-mail address: `haizhao@math.duke.edu`

DEPARTMENT OF MATHEMATICS, DEPARTMENT OF PHYSICS, AND DEPARTMENT OF CHEMISTRY,
DUKE UNIVERSITY, BOX 90320, DURHAM NC 27708, USA
E-mail address: `jianfeng@math.duke.edu`